Article

Heterostructure Films of SiO₂ and HfO₂ for High-Power Laser Optics Prepared by Plasma-Enhanced Atomic Layer Deposition

Shawon Alam [1,2], Pallabi Paul [1,2], Vivek Beladiya [1,2], Paul Schmitt [1,2], Olaf Stenzel [2], Marcus Trost [2], Steffen Wilbrandt [2], Christian Mühlig [2], Sven Schröder [2], Gabor Matthäus [1], Stefan Nolte [1,2], Sebastian Riese [3], Felix Otto [4], Torsten Fritz [4], Alexander Gottwald [5] and Adriana Szeghalmi [1,2,*]

1   Institute of Applied Physics, Abbe Center of Photonics, Friedrich Schiller University Jena, Albert-Einstein-Str. 15, 07745 Jena, Germany
2   Fraunhofer Institute for Applied Optics and Precision Engineering, Albert-Einstein-Str. 7, 07745 Jena, Germany
3   Layertec GmbH, Ernst-Abbe-Weg 1, 99441 Mellingen, Germany
4   Institute of Solid State Physics, Faculty of Physics and Astronomy, Friedrich Schiller University Jena, Helmholtzweg 5, 07743 Jena, Germany
5   Physikalisch-Technische Bundesanstalt, Abbestraße 2-12, 10587 Berlin, Germany
*   Correspondence: adriana.szeghalmi@iof.fraunhofer.de; Tel.: +49-3641-807-320

Abstract: Absorption losses and laser-induced damage threshold (LIDT) are considered to be the major constraints for development of optical coatings for high-power laser optics. Such coatings require paramount properties, such as low losses due to optical absorption, high mechanical stability, and enhanced damage resistance, to withstand high-intensity laser pulses. In this work, heterostructures were developed by sub-nanometer thin films of SiO₂ and HfO₂ using the plasma-enhanced atomic layer deposition (PEALD) technique. Thin-film characterization techniques, such as spectroscopic ellipsometry, spectrophotometry, substrate curvature measurements, X-ray reflectivity, and Fourier transform infrared spectroscopy, were employed for extracting optical constants, residual stress, layer formation, and functional groups present in the heterostructures, respectively. These heterostructures demonstrate tunable refractive index, bandgap, and improved optical losses and LIDT properties. The films were incorporated into antireflection coatings (multilayer stacks and graded-index coatings) and the LIDT was determined at 355 nm wavelength by the R-on-1 method. Optical absorptions at the reported wavelengths were characterized using photothermal common-path interferometry and laser-induced deflection techniques.

Keywords: heterostructures; plasma-enhanced atomic layer deposition; LIDT; silicon dioxide; hafnium dioxide; antireflection coatings; low-loss coating

1. Introduction

Research on optical coatings for high-power laser optics in the ultraviolet and near-infrared spectral range has long been the center of attention due to scarcity of thin-film materials that are transparent or experience low absorption and exhibit high damage resistance in such spectral ranges [1,2]. Laser-induced damage threshold (LIDT) is a major constraint for developing such coatings for high-power laser systems as the optics experience damage upon high-intensity laser irradiation [3–6]. Several oxides, such as TiO₂, Nb₂O₅, ZrO₂, Ta₂O₅, HfO₂, Sc₂O₃, Al₂O₃, SiO₂, and various fluorides, are prevalent materials for multilayer optical coatings comprised of alternating low- and high-refractive-index material [7–10]. Among these materials, HfO₂ is a promising high-refractive-index substance that has attracted much attention on account of its exclusive properties, such as a wide bandgap (5.5–5.7 eV), thermal stability, high laser damage resistance, and a broad transparency range from ultraviolet to mid-infrared (0.22–12 μm) [11–15]. HfO₂ films are also preferred to replace SiO₂ as gate dielectric oxides in semiconductor applications

due to their high dielectric constant (25–28), density, and ductility [12,16–20]. SiO_2 is known as a prominent low-refractive-index material used for high-power laser coatings from the ultraviolet to infrared spectral range because of its broad transparency range (0.2–8 μm) [21–23]. Silica films exhibit a dielectric constant of approximately 3.9, and a large optical bandgap (8.9–9.0 eV) [14,18,24–26]. SiO_2 finds applications in microelectronic devices as a gate insulator and in photovoltaics [17,25,27–30]. Most of these films have optical absorption near the ultraviolet spectral region, limited by the width of the bandgap but also defects that broaden the valence and conduction bands [1,7]. These oxides also have specific refractive index values, but some applications require intermediate values for optimal performance. Finding materials with suitable optical characteristics (high LIDT and low absorption losses) for high-power laser coatings in the UV spectral range is a great challenge because such materials are limited.

Atomically mixing low- and high-index materials from these sets of oxides to realize heterostructures provides new capabilities to produce thin films with tunable refractive index, residual stress, and optical bandgap, which can expand the current application types [31–36]. HfO_2, as a high-index material, is usually combined with the low-refractive-index oxide SiO_2 to form multilayer coating, which can exhibit intermediate refractive indices between those of the constituents and achieve reduction in optical losses due to extension of the transparent spectral range down to the deep UV spectral range [14,26,37]. Heterostructures can also tune laser damage resistance due to modified optical bandgap values, as reported by Gallais et al. [8]. Among other heterostructures (high- and low-index combinations), SiO_2:HfO_2 composites are promising for optical coatings because of their thermomechanical stability and high LIDT [1,38–40].

Graded-index coatings have been observed to achieve enhanced film properties and laser damage resistance due to reduction in discontinuous interfaces [34,41]. Such coatings are also called rugate or inhomogeneous coatings and consist of continuously varying refractive index n, along with the film thickness rather than an abrupt change in n, as in discrete multilayer stacks [41–43]. However, a varying refractive index can be obtained by adjusting the composition of the heterostructure's constituent materials at the atomic level [9,44]. Graded-index coatings can substantially reduce reflectance by matching the intermediate refractive indices between the substrate and the air medium [26,45,46].

An amorphous state of the thin film is desired in optical coatings because crystalline films generate grain boundaries which lead to losses due to scattering and absorption [26,47,48]. HfO_2 films tend to crystallize at a relatively low deposition temperature, as reported by several authors [49,50]. The previous work from our group reported on the thickness and temperature-dependent crystallinity of pure HfO_2 [51]. The heterostructures can also mitigate crystallization by incorporating a thin layer of an amorphous film within such coatings [44,48,52]. Inclusion of SiO_2 in HfO_2 films can significantly increase the crystallization temperatures of HfO_2 to much higher ranges, which means the film can retain the amorphous state up to a higher temperature [26,53].

Deposition of heterostructure coatings is quite challenging because the film requires versatile properties, such as low absorption losses, enhanced mechanical stability, and high damage resistance, to withstand intense laser irradiation. Electron beam evaporation (EBE), ion-beam sputtering (IBS), ion-assisted deposition (IAD), sol–gel methods, and chemical vapor deposition (CVD) are often applied for high-power laser optical coatings [5,12,15,47]. Atomically thin heterostructure compositions are difficult to process with these techniques. Additionally, for 3D photonic integration, it is essential to ensure atomic-scale precision along with 3D conformality on arbitrary substrate geometries. Atomic layer deposition (ALD) is a powerful technique for preparing optical coatings for high-power laser optics that enables deposition at a lower temperature using variant plasma-enhanced ALD [1,25,54,55]. ALD is based on two self-limiting surface reactions that provide atomic-scale control over the film thicknesses and conformal growth along complex-shaped substrates, which are suitable for high-power laser components, such as aspheric lenses, laser mirrors, beam expanders, polarizers, and beam splitters, for industrial applications [12,16,31,56,57]. ALD-

grown films are homogeneous, smooth, highly dense, and pinhole-free, exhibiting high resistance to laser-induced damage [1,47,58,59].

This work intends to provide a comprehensive understanding of SiO_2:HfO_2 heterostructure films prepared by the plasma-enhanced atomic layer deposition (PEALD) process. The heterostructure films were analyzed by employing several state-of-the-art characterization techniques to understand the tunability of various properties as well as realizing coatings for high-power laser applications.

2. Materials and Methods

2.1. Deposition of SiO_2:HfO_2 Thin-Film Heterostructures

Single-layer thin films of SiO_2, HfO_2, and SiO_2:HfO_2 heterostructures (with varying composition ratio of SiO_2 and HfO_2) were fabricated using a SILAYO-ICP330 PEALD reactor (Sentech Instruments GmbH, Berlin, Germany) [12,60]. Such instruments incorporate an inductively coupled plasma source (RF generator, 13.56 MHz, up to 500 W) with the possibility of implementing both thermal and plasma-enhanced ALD processes. Thin films of SiO_2 and HfO_2 were prepared using the bis[diethylamino]silane (BDEAS) and tetrakis-dimethylamino hafnium (TDMAH) precursors on fused silica (FS, diameter 25 mm, thickness 1 mm) and silicon wafer substrates. The film growth depends on several process parameters, such as growth temperature, precursors' pulse-purge duration, and the flow rate of carrier gases affecting the material properties of the films [61,62]. Process parameters for SiO_2 and HfO_2 films were previously optimized to ensure reproducible growth and good film thickness uniformity [51,60]. The process parameters of the PEALD thin-film depositions are listed in Table 1.

Table 1. PEALD process parameters for SiO_2:HfO_2 heterostructure films.

Thin Films	Precursor Pulse | Purge (s)	Co-Reactant Pulse | Purge (s)	O_2 Flow (sccm)	Ar Flow (sccm)
SiO_2	BDEAS: $SiH_2(N(CH_2CH_3)_2)_2$ 0.32 | 5	O_2 Plasma 3 | 2	200	30
HfO_2	TDMAH: $Hf(N(CH_3)_2)_4$ 3 | 5	O_2 Plasma 5 | 5	200	160

sccm: standard cubic centimeter per minute.

The deposition temperature was kept at 100 °C for all the processes within the framework of this work to suppress temperature-dependent crystallization of HfO_2 thin films. The plasma power was kept at 100 W. The precursor pulse and purge times for SiO_2 and HfO_2 was different because of different vapor pressures and chemical reactivity of the precursors [30,44]. Argon was utilized as both precursor carrier and purge gas for these films. The purge steps are applied to prevent gas-phase reactions between the precursors (reactant) and co-reactant (oxidant agent) in the reactor [30,44,63].

2.2. Characterizations of the SiO_2:HfO_2 Heterostructure Films

Several analytical techniques have been applied to characterize the PEALD thin films for extracting optical constants (refractive index and extinction coefficient), film thickness, spectral performance (reflectance, transmittance, optical losses), mechanical stress, surface roughness, composition, and laser-induced damage threshold. Optical constants and thickness of the films grown on Si-(100) substrates were estimated by spectroscopic ellipsometry measurements using a variable angle ellipsometer (Sentech Instruments GmbH, Berlin, Germany). A Tauc–Lorentz-oscillator-model-based approach was implemented to determine the optical constants of the heterostructures by fitting the measured ellipsometric parameters. Further, the indirect optical bandgap of such structures is estimated using Tauc-plot calculations.

The reflectance R and transmittance T spectra were measured using a spectrophotometer device (Lambda 950, PerkinElmer Inc., Waltham, MA, USA) from 190 to 1200 nm wavelength within a measurement accuracy of $\pm$0.3%. The optical losses (OL) are calculated using the following expression [64–66]: OL = 1-T-R.

In order to extract the optical constants of the heterostructures in the vacuum ultraviolet (VUV) spectral ranges, further T/R measurements were carried out between 125 and 225 nm at 2° angle of incidence at the Physikalisch Technische Bundesanstalt, Berlin [67,68]. The measurement uncertainties in the VUV range were between 0.8% and 1.2%. The optical constants were further extracted from the VUV transmittance and reflectance spectra using a Lorentzian calculator (LCalc) [64].

The mechanical stress of the heterostructures was estimated using an FLX-2320 instrument (KLA-Tencor GmbH, Dresden, Germany) based on measurement of the change in radius of curvature of the substrate before and after deposition of the PEALD films. The stress values in the films are calculated from these substrate curvature measurements using the Stoney equation [69–71]:

$$\sigma = \frac{1}{6} \cdot \frac{E_s}{(1 - \nu_s)} \cdot \frac{t_s^2}{t_f} \left(\frac{1}{R_f} - \frac{1}{R_s} \right)$$

where σ is the mechanical stress, t_s and t_f are substrate and film thickness, R_s and R_f are the radius of curvature of the bare (substrate without film before deposition) and coated wafer (substrate with film after deposition). E_s and ν_s indicate Young's modulus and Poisson's ratio of the substrate, respectively.

X-ray reflectivity (XRR) measurements were conducted on FS and Si wafers to estimate the thickness, surface roughness, intermixing, and layer densities of the oxides in the heterostructure films [30,72]. The XRR instruments (Bruker AXS, Karlsruhe, Germany) consist of a monochromatic X-ray beam (Cu-Kα radiation at λ = 0.154 nm) for such measurements at grazing incident angle from 0° to 8° [73]. The measured spectra were fitted using Brucker Leptos 7 software for obtaining the film properties [72].

Fourier transform infrared spectroscopy (FTIR) (Varian Inc., Palo Alto, CA, USA) for heterostructures on Si wafers was performed to investigate functional groups present in the films [63,74]. This technique utilized mid-infrared radiation (from 400 to 4000 cm^{-1}) exciting molecular vibrations [63,75], and the spectra were baseline corrected.

AFM measurements were conducted on selected heterostructures to further investigate their surface roughness. A Dimension 3100 (Bruker, Billerica, MA, USA) equipped with a Nanoscope controller (Digital Instruments, Tonawanda, NY, USA) was used at ambient conditions. The AFM tips had a typical radius of less than 10 nm. Sample areas of 1×1 μm^2 and 2×2 μm^2 were scanned in tapping mode, and their surface roughness was calculated as root-mean-square (rms).

Laser-induced damage threshold (LIDT) tests of the heterostructure films on fused silica substrates were performed using high-intensity laser irradiation of nanosecond pulses. The ISO-21254 standard framework defines LIDT as the maximum quantity of laser fluence or energy density optics can withstand for which the extrapolated probability of damage is zero [76,77]. The R-on-1 test method was deployed using a Nd:YAG frequency-tripled, Q-switched LITRON NanoTRL-650-10 laser (Litron Lasers, Rugby, UK) in order to estimate the LIDT of the coatings. The effects of linear absorption on the LIDT of the heterostructure films were estimated by employing the photothermal common-path interferometry (PCI) method. These measurements were carried out on fused silica substrates at 355 nm wavelength.

3. Results

Single-layer thin films of SiO$_2$ and HfO$_2$ on Si wafers were prepared by the PEALD processes before proceeding toward heterostructures. Spectroscopic ellipsometry was employed to determine thicknesses for such films. The growth per cycle (GPC) of the films was estimated through dividing the thicknesses by the number of cycles applied. HfO$_2$ films exhibit relatively higher GPC (1.70 Å/cycle) compared to SiO$_2$ (1.17 Å/cycle) [12,56,57,78].

The refractive indices of SiO_2 and HfO_2 are reported at 355 and 1064 nm wavelengths. High-index HfO_2 film exhibits 2.01 at 355 nm and 1.93 at 1064 nm wavelengths, whereas SiO_2 marked 1.47 at 355 nm and 1.45 at 1064 nm wavelengths as the refractive indices. These results are consistent with the refractive indices, with a little deviation (due to different deposition methods and process parameters) reported by other authors [50,79,80]. The knowledge obtained from the single-layer thin films was then applied to deposition of heterostructures.

The heterostructures were prepared from the alternating layers of SiO_2 and HfO_2 films with a specific number of bilayers to realize a half-wave optical thickness at 1064 nm wavelength [40,81–83]. However, ultrathin layers of the heterostructures (approximately 25 nm) were grown at the beginning to estimate the GPC and refractive indices at the target wavelength. The composition, total thickness, and refractive indices of a series of heterostructures deposited on the Si wafer and fused silica substrates are shown in Table 2. The heterostructure films were categorized into several groups with gradually increasing cycles of HfO_2 for 2, 4, 8,16, and 64 cycles of SiO_2.

Table 2. The composition, total thickness, and refractive indices of SiO_2:HfO_2 heterostructures.

Sample ID	ALD Cycles of SiO_2	ALD Cycles of HfO_2	Cycle Ratio SiO_2:HfO_2	Number of Bilayers	Thickness (nm) $\pm$ 0.1	Refractive Index (355 nm) $\pm$0.01	Refractive Index (1064 nm) $\pm$0.01
S1	2	2	1:1	615	307.1	1.83	1.76
S2	2	8	1:4	100	149.5	1.99	1.90
S3	2	16	1:8	98	293.3	2.01	1.92
S4	4	2	2:1	465	325.1	1.71	1.66
S5	4	4	1:1	315	323.6	1.82	1.75
S6	4	8	1:2	160	275.8	1.91	1.83
S7	4	16	1:4	87	271.1	1.97	1.88
S8	8	2	4:1	300	342.3	1.62	1.58
S9	8	4	2:1	230	324.8	1.73	1.67
S10	8	8	1:1	145	301.3	1.83	1.76
S11	8	16	1:2	76	260.6	1.93	1.84
S12	16	16	1:1	72	301.5	1.84	1.77
S13	64	2	32:1	20	160.5	1.50	1.47
S14	64	4	16:1	20	166.7	1.52	1.49
S15	64	8	8:1	20	180.7	1.57	1.53
S16	64	16	4:1	20	200.4	1.66	1.61

For example, the first group incorporates sample S1 to S3, which comprise two cycles of SiO_2 with 2, 8, and 16 cycles of HfO_2. Several heterostructures (S1, S5, S10, and S12) were emboldened in the table as they belong to identical cycle ratio groups with different numbers of cycles of the constituents. These samples have nearly identical refractive indices. Overall, the refractive indices of the heterostructures varied at the reported wavelengths (355 and 1064 nm) due to their composition and stayed between SiO_2 and HfO_2. The film thickness and optical constants were extracted through the Tauc–Lorentz model upon fitting the ellipsometry spectra (Ψ and Δ, generated at a 70° angle of incidence from 200 to 980 nm wavelength in ambient environment). The oscillator dispersion model consists of several fit parameters, such as amplitude, center energy, broadening, and optical bandgap. Representatives of heterostructures with four and eight cycles of SiO_2 are shown in Figure 1a–d. The curves (measured and simulated) were in very good agreement for Ψ and Δ. The Ψ and Δ for each heterostructure were slightly shifted spectrally with respect to each other due to the composition-dependent optical properties. Therefore, the Tauc–Lorentz dispersion relation demonstrated quite good results for estimating optical constants and film thicknesses of the heterostructures.
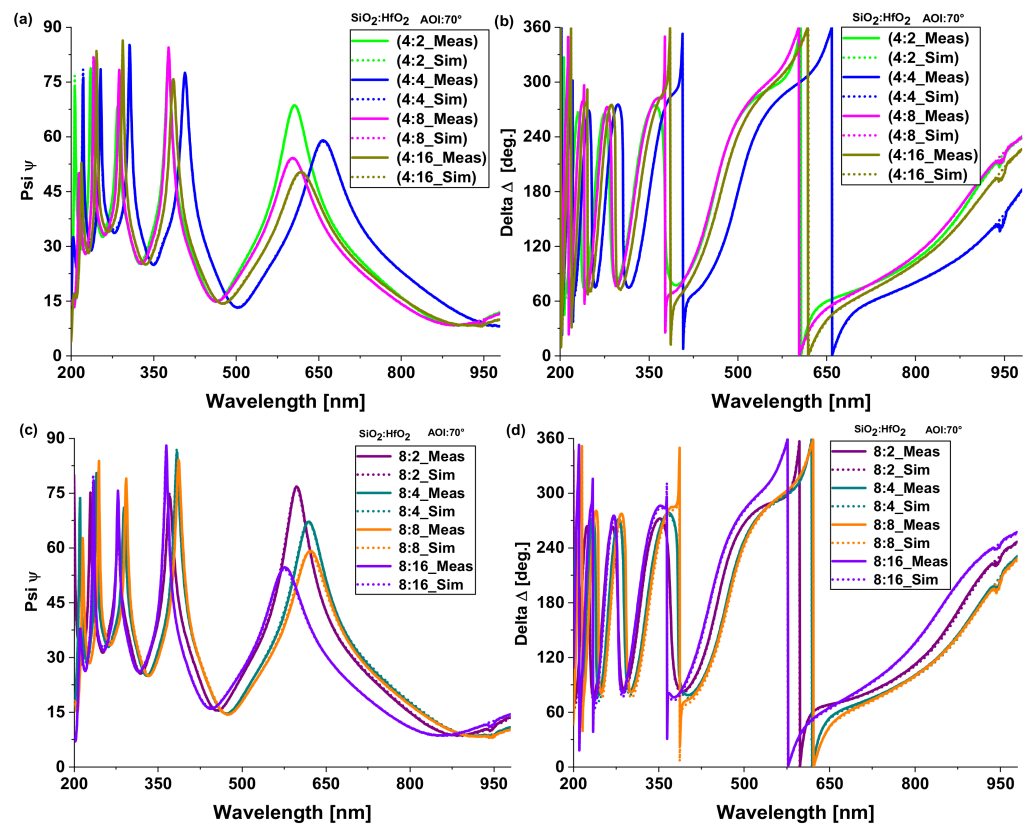
Figure 1. Measured and simulated spectroscopic ellipsometric parameters (Ψ and Δ) for the SiO$_2$:HfO$_2$ heterostructures with (**a**,**b**) 4 and (**c**,**d**) 8 cycles of SiO$_2$.

The composition-dependent optical constants (*n*, *k*) obtained through a Tauc–Lorentz dispersion relation for SiO$_2$:HfO$_2$ heterostructures are included in Figure 2a–f, where the curves were reported between 200 and 1100 nm wavelength. It is evident from Figure 2a–c that their dispersion curves take values between HfO$_2$ and SiO$_2$, meaning the intermediate refractive indices are obtainable from the heterostructures by atomically adjusting the constituents. These intermediate indices are usually not achievable from a single material, as no films exist with such refractive indices in nature, providing flexibility in the thin-film coatings design, which broadens the application window. In Figure 2b,c, the refractive indices curves of ultrathin layers of the heterostructures with four and eight cycles of SiO$_2$ are also included along with thick films. There is typically a good agreement between the optical properties of thin and thick films with identical composition, but some variations are attributed to the inaccuracy of the thin film analysis. The refractive index values of the heterostructures corresponding to Figure 2a–c are reported in Table 2 for the two specific wavelengths, e.g., 355 and 1064 nm, respectively. The extinction coefficient curves of the heterostructures in Figure 2d–f show that the absorption edge of HfO$_2$ is located nearly at 230 nm wavelength. However, the absorption edges for SiO$_2$ along with some heterostructures could not be determined due to the spectral limitation of the ellipsometer. The absorption edge is gradually shifting toward shorter wavelengths because of the heterostructures' composition, leading to quantizing effects on the energy states.
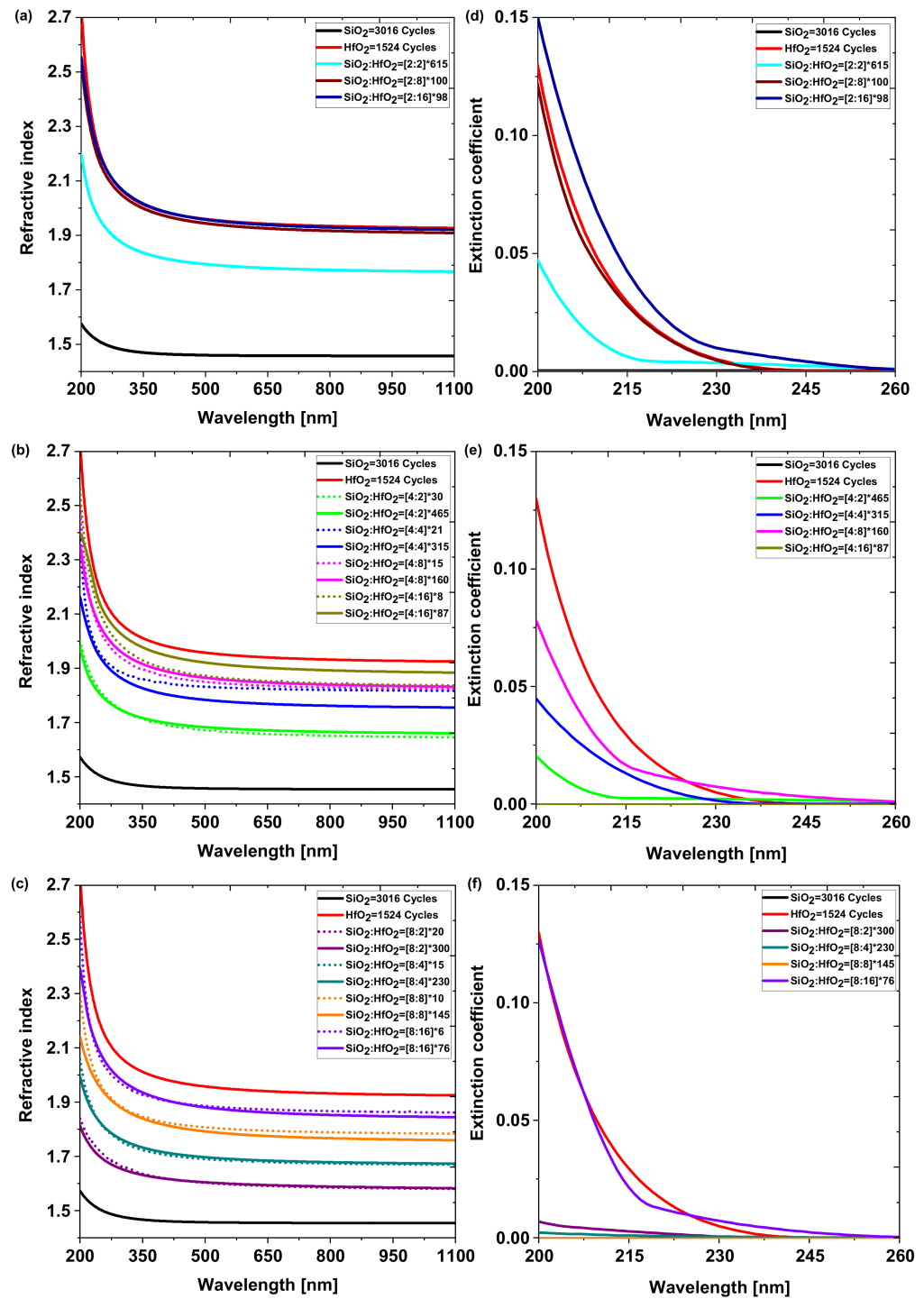
Figure 2. Optical constants for the heterostructures with (**a**,**b**) 2, (**c**,**d**) 4, and (**e**,**f**) 8 cycles of SiO_2.

The dispersion profile of the heterostructures with identical cycle ratio are illustrated in Figure 3. They exhibit reasonably similar refractive indices, as shown in Figure 3a. The extinction coefficient profiles in Figure 3b indicate some variation of the extinction coefficient among heterostructures with identical composition ratio. This feature can be attributed to a change in stoichiometry of the HfO_2 layer. As SiO_2 films become extremely thin, they tend to donate oxygen, which could be diffused to the adjacent HfO_2 layer while compensating for the stoichiometry and reducing the extinction values. However, it does not appear that the number of interfaces in the heterostructures influences the extinction spectra. The absorption edge of HfO_2 is located near at 230 nm wavelength. The slight blue

shift in extinction coefficients upon decreasing the number of ALD cycles of SiO_2 and HfO_2 while keeping the cycle ratio unchanged might be an indication of the quantum size effect. Such effects were reported for Al_2O_3:TiO_2 ALD heterostructures in our previous work [84].
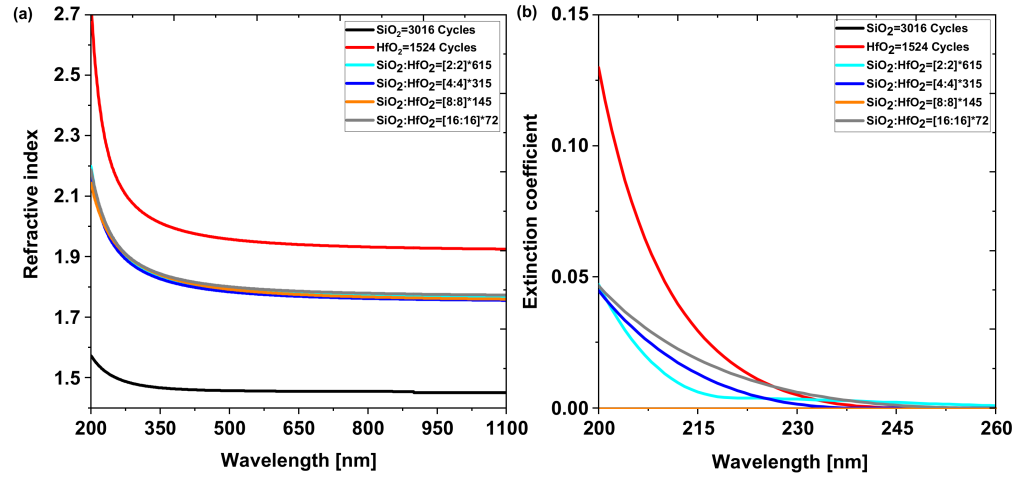

Figure 3. Optical constants ((**a**) refractive indices and (**b**) extinction coefficients) for the heterostructures with identical cycle ratios of the constituents.

To estimate the optical constants of the heterostructures in vacuum ultraviolet (VUV) ranging from 125 to 225 nm in wavelength, heterostructures with four and eight cycles of SiO_2 were selected for the measurements. The optical constants extracted from VUV together with UV–vis ranges are shown in Figure 4a–d. The spectra obtained from the VUV measurements (dotted curves) are consistent with the UV–vis observed trend (solid curves). However, the slight variation between the values in the overlap spectral range could be attributed to a vacuum-to-air shift or measurement and fitting uncertainties.
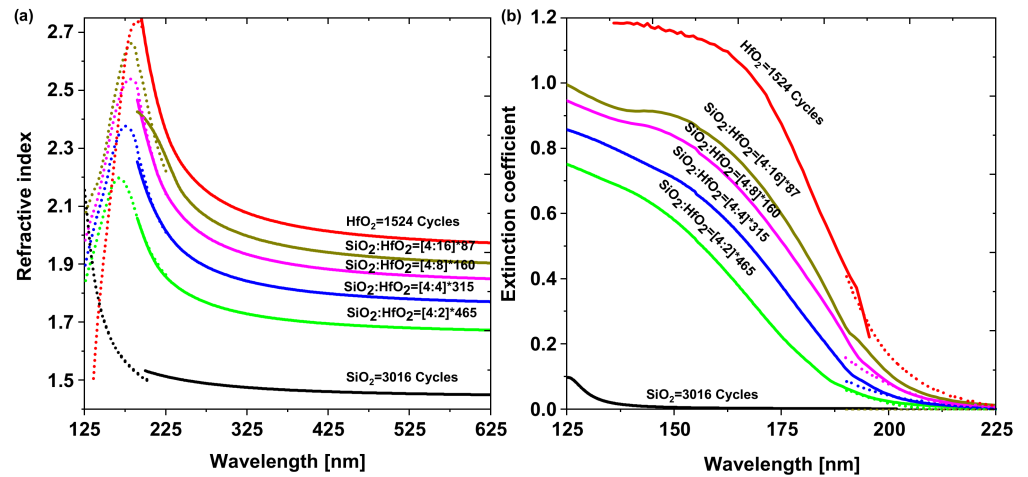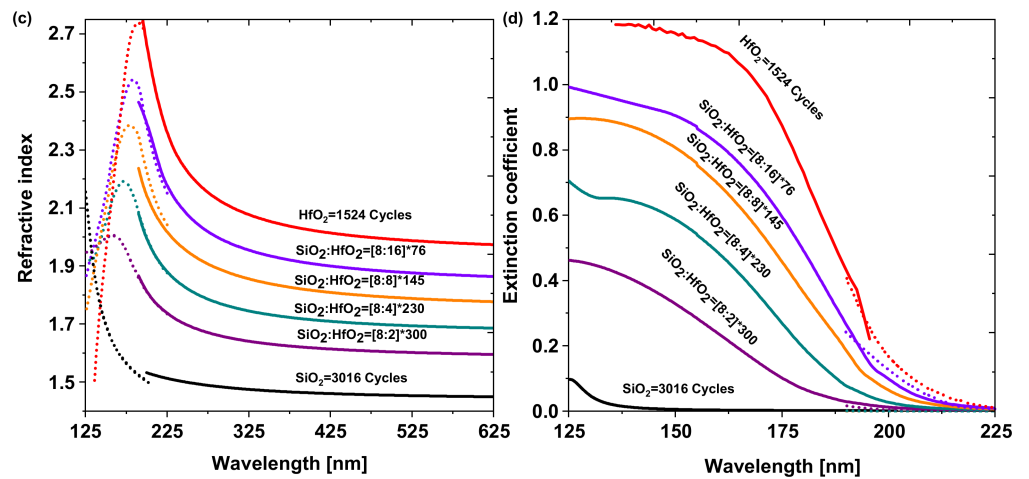

Figure 4. *Cont.*

Figure 4. Comparison of optical constants as a function of wavelength estimated from VUV and UV–vis measurements for (**a**,**b**) 4 and (**c**,**d**) 8 cycles of SiO$_2$.

The optical bandgap values of SiO$_2$ and HfO$_2$ were estimated by Tauc plot calculations to be at 8.9 and 5.6 eV, respectively. These values are also consistent with literature values; however, they deviate slightly depending on the applied deposition methods [11,15,25]. The bandgap values of heterostructures with two, four, and eight cycles of SiO$_2$ were also estimated and graphically represented with refractive indices at a wavelength of 355 nm in Figure 5. The optical bandgap values follow an inverse relationship with the refractive index. The bandgaps of the heterostructures are controlled by HfO$_2$ since inclusion of more SiO$_2$ content in the heterostructures enhances the bandgap. The heterostructures with identical cycle ratios, e.g., [2:2]*615, [4:4]*315, and [8:8]*145, exhibit similar values of refractive indices within their determination accuracy; however, their optical bandgap can be tailored to a certain extent (for instance, here, 5.6–5.9 eV) depending on their individual layer thicknesses. The increase in the optical bandgap is attributed to electron confinement due to quantizing well-barrier structures.
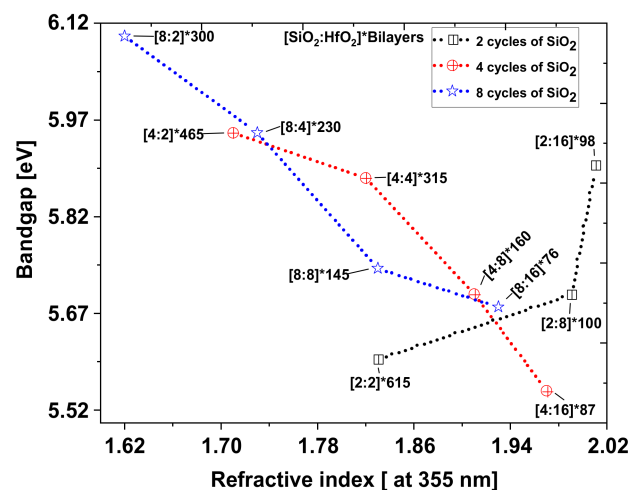

Figure 5. Optical bandgap as a function of refractive index at 355 nm wavelength.

HfO$_2$ is transparent down to approximately 250 nm wavelength, while SiO$_2$ shows transparency for a broad spectral range between deep UV and NIR spectral range. Creating the heterostructures enables enhanced optical properties, such as extended transparency range, depending on the composition of the two constituents. Figure 6 displays the transmission *T*, reflection *R* and optical losses spectra of the SiO$_2$:HfO$_2$ heterostructures with identical cycle ratios. The deviations in transmission maxima and reflection minima

for the compositions in Figure 6a can be attributed to the difference in their total physical thickness. In Figure 6b, single-layer HfO_2 film exhibits higher losses in the UV spectral range due to its optical absorption edge. Therefore, this optical absorption edge can also be tailored by atomically controlling thickness of HfO_2 films through precise tuning of composition, enabled by PEALD. Optical losses curves in Figure 6b indicate a shift in the absorption edges toward shorter wavelengths due to a decrease in interlayer thickness (i.e., decreasing PEALD cycles of SiO_2 and HfO_2 while keeping the cycle ratios constant), attributed to quantum size effects. Such trends are also consistent with the extinction coefficient curves, as shown in Figure 3b.
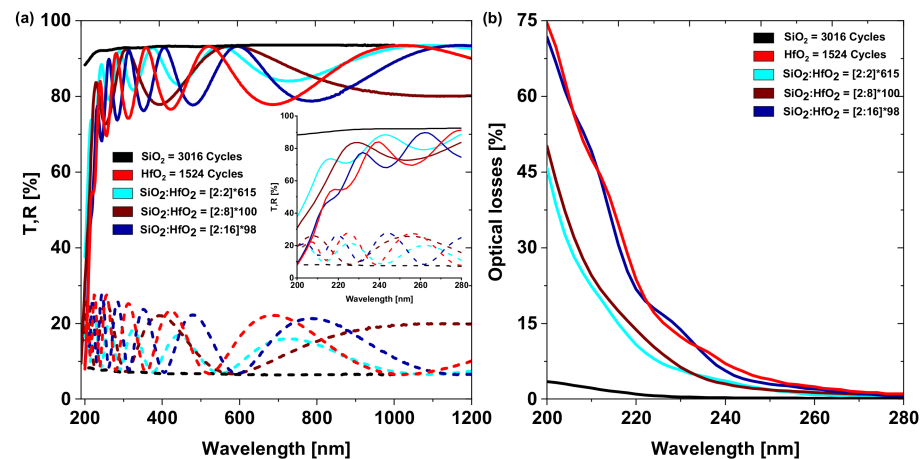

Figure 6. (**a**) Transmittance T (solid curves), reflectance R (dashed curves), and (**b**) optical losses spectra for the SiO_2:HfO_2 heterostructures with increasing HfO_2 content.

Additionally, the T and R spectra of the heterostructures with four and eight cycles of SiO_2 were also measured in the VUV spectral range due to shifting in the absorption edge upon enhanced film properties. The spectra measured in the VUV range are graphically plotted along with the UV–vis measurements in Figure 7. Some spectral shifts could also be associated with measurements at 2° and 6° angles of incidence for the VUV and UV–vis ranges, respectively. Nevertheless, the spectra were consistent with the trend observed through both measurement ranges.
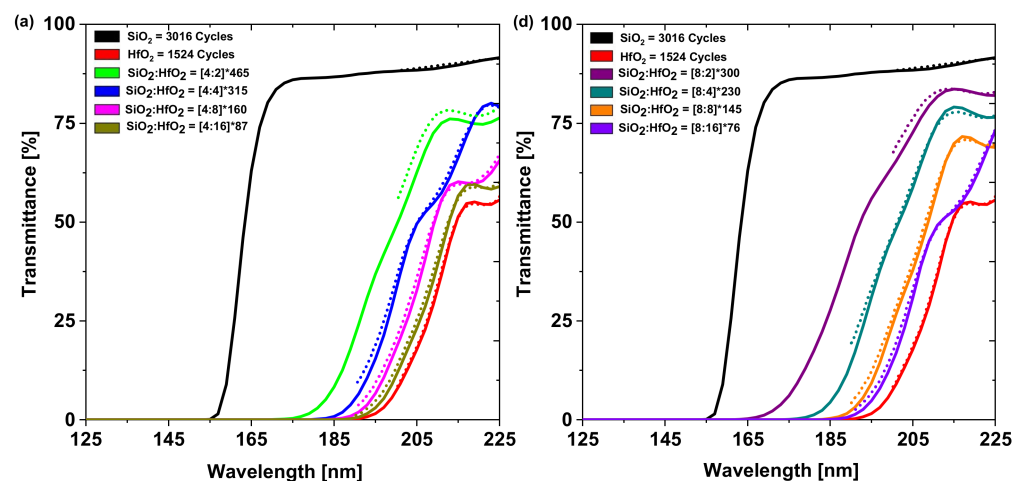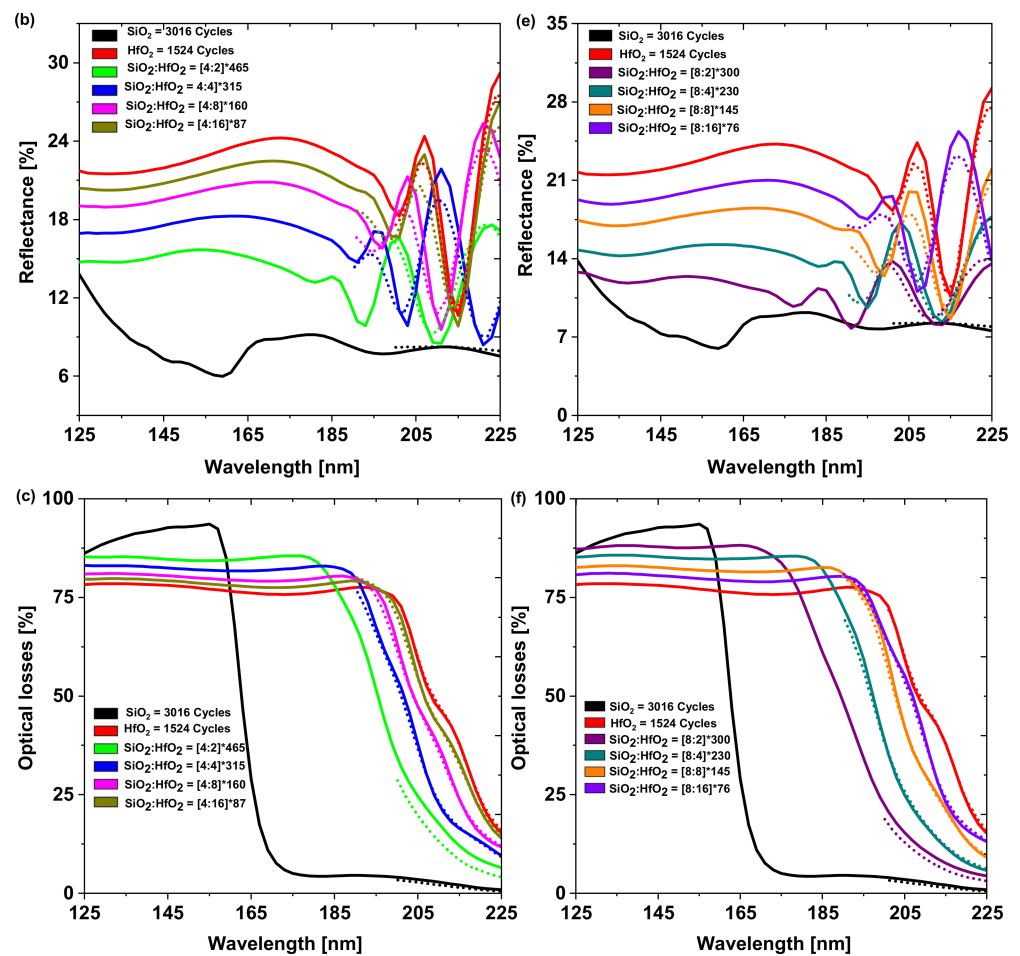

Figure 7. *Cont.*

Figure 7. Transmittance *T*, reflectance *R*, and optical losses spectra of SiO$_2$:HfO$_2$ heterostructures with (**a**–**c**) 4 and (**d**–**f**) 8 cycles of SiO$_2$ in the vacuum ultraviolet spectral ranges (dotted curves UV–vis, solid curves VUV data).

Manipulating the mechanical stress of multilayer films is crucial for their stability. The mechanical strengths of the heterostructures are reported for two, four, eight, sixteen, and sixty-four cycles of SiO$_2$ with increasing cycles of HfO$_2$. The residual stresses of such films were estimated by the wafer curvature measurement technique and graphically represented in Figure 8. It was observed that the mechanical stress of the heterostructures can be controlled by adjusting the thickness of the ALD interlayers. The heterostructures with two, four, eight, and sixteen cycles of SiO$_2$ exhibit tensile stress between 250 and 635 MPa. Heterostructures with identical cycle ratios of constituents, such as [2:2]*615, [4:4]*315, [8:8]*145, and [16:16]*72, reveal increasing stress due to the increase in HfO$_2$ thickness. However, heterostructures with 64 cycles of SiO$_2$ are quite complex and require further investigation as the films express tensile and compressive stresses. The residual stress for these heterostructures increases because of gradual inclusion of more HfO$_2$ in the composition. However, the stress in the film should be optimized because the high coating stress might lead to functional degradation, especially for complex interference coating systems.
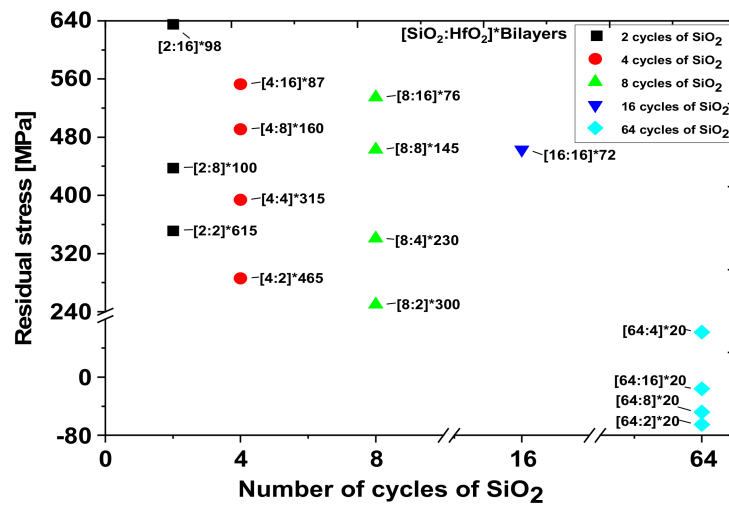
Figure 8. Residual stress values of the SiO$_2$:HfO$_2$ heterostructure coatings.

3.1. X-ray Reflectivity Analysis

X-ray reflectivity (XRR) analysis of SiO$_2$:HfO$_2$ heterostructures was conducted on Si substrates at grazing angles (0° to 8°) to estimate the layer properties, such as thickness, density, intermixing at interfaces, and surface roughness of the heterostructures. A schematic diagram of the SiO$_2$:HfO$_2$ heterostructures is depicted in Figure 9a. The measured and simulated curves of the SiO$_2$:HfO$_2$ films for a different number of ALD cycles of the constituent oxides denoting identical cycle ratios are presented in Figure 9b.
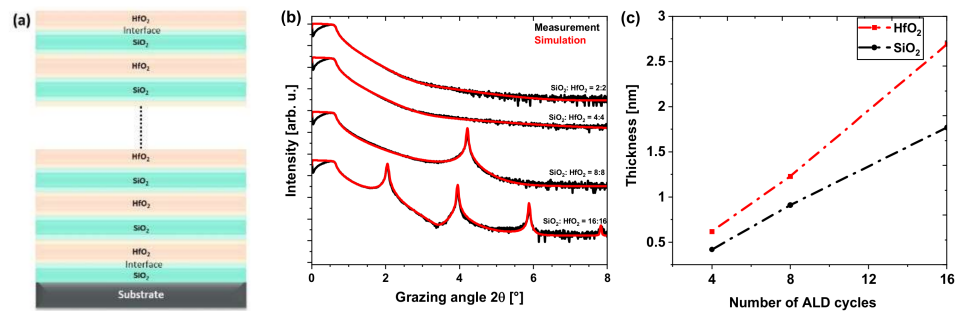

Figure 9. (**a**) Schematic representation of SiO$_2$:HfO$_2$ heterostructures by PEALD, (**b**) measured and simulated X-Ray reflectivity curves of SiO$_2$:HfO$_2$ heterostructures grown on FS, and (**c**) constituent layers thickness variation as a function of PEALD cycles.

Intermixing at the interfaces was estimated by including roughness at each of the SiO$_2$–HfO$_2$ interfaces. This roughness was approximately 0.5 nm. The measured curves (black) show very good agreement with the simulated spectra (red). The reflectivity curves show the presence of sharp Bragg peaks, i.e., indicating superlattice characteristics, for the SiO$_2$:HfO$_2$ [8:8] and [16:16] heterostructures, where the layer thickness for SiO$_2$ was 0.9 nm and 1.77 nm, respectively. The layer thickness of HfO$_2$ for the heterostructures was recorded as 1.23 nm and 2.69 nm, which was higher than that of SiO$_2$. The heterostructures are amorphous by nature. The Bragg peaks in the XRR measurements in Figure 9b indicate layer-by-layer growth of the heterostructures. As the individual layer thickness of HfO$_2$ and SiO$_2$ decreases to a sub-nanometer scale, the Bragg peaks disappear, for instance, the structure with [2:2] PEALD cycle ratios in Figure 9b, where a ternary oxide is probably formed. A weak Bragg peak is observed for the [4:4] composition grown on Si wafer at around 8.47° (not shown) but not on FS substrate, indicating the role of the substrate on heterostructure formation. The intermixing (roughness layers) was also typically larger for films grown on FS than on Si substrates.

It was observed that the layer thickness of the constituents increased almost two-fold when the number of ALD cycles doubled. ALD provides controlled growth of heterostructure films down to atomic scale by adjusting cycle ratio numbers. The periodic motifs for other heterostructures were not detected at the grazing incident angle because the peaks of the curves disappear due to a decrease in bilayer thickness. Layer thickness as a function of ALD cycles is depicted in Figure 9c. The GPC of HfO_2 and SiO_2 can further be estimated from the slope of Figure 9c. The GPC of HfO_2 was higher than SiO_2 for the heterostructures due to the precursor properties. The total thickness of the heterostructures estimated by XRR was in good agreement with the spectroscopic ellipsometry analysis demonstrated in Table 2. For the increasing number of ALD cycles, the density of HfO_2 film increased from 8.25 to 8.5 gcm^{-3} compared to that of SiO_2, from 2.2 to 2.3 gcm^{-3}. The surface roughness of HfO_2 remained around 0.3–0.5 nm. Therefore, small surface roughness and HfO_2 density represent the amorphous state of the heterostructures because crystalline HfO_2 films exhibit high densities and rough surfaces due to columnar growth characteristics [19,21,85,86].

3.2. Fourier Transform Infrared Spectroscopy (FTIR) Analysis

The SiO_2:HfO_2 heterostructures along with single-layer SiO_2 and HfO_2 were investigated by the FTIR technique to identify the functional groups present in the films. The FTIR spectra were measured from 400 to 4500 cm^{-1} ranges (Figure 10a,b). The different peaks in the spectra are identified as fingerprints of bonds and functional group regions of the films. The FTIR spectra were thickness-normalized to make the peaks comparable for each film material. The normalized thickness was chosen to be 300 nm as most of the heterostructures were nearly in this thickness range. The FTIR peaks found in the curves were compared with those in the literature and denoted in Figure 10.
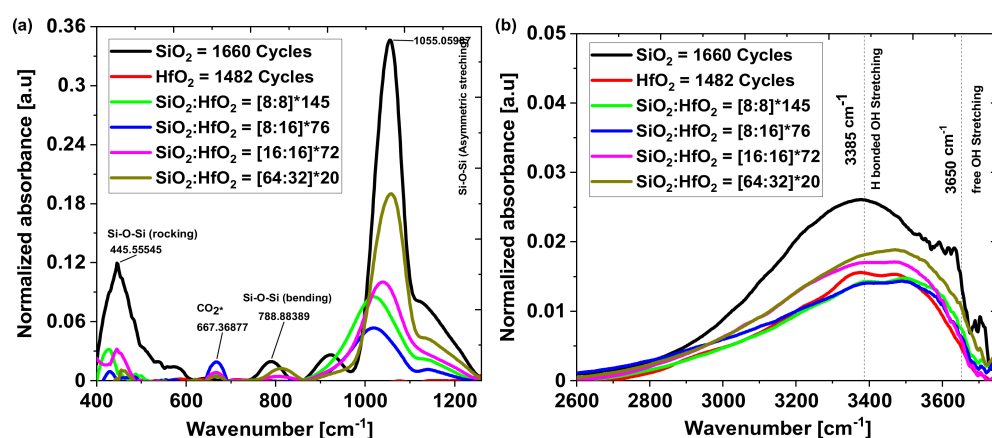

Figure 10. FTIR absorption spectra of the heterostructures from (**a**) 400 to 1200 cm^{-1} and (**b**) 2600 to 3750 cm^{-1}.

Three different vibrational modes of SiO_2 were detected at 446, 788, and 1055 cm^{-1}, respectively [60,87]. However, no peaks for HfO_2 films were encountered as the features of HfO_2 exceed our measurement ranges and the signal intensities were very low [53,87]. The SiO_2 films incorporate more OH groups compared to HfO_2, as shown in Figure 10b. Two major absorption peaks were detected for the heterostructures at 3385 and 3650 cm^{-1} for different OH stretching modes [87,88]. The heterostructures were in good agreement with the findings of their constituents at 3650 cm^{-1} as the film with significant influence of SiO_2 exhibits more OH groups, e.g., for heterostructures with 64 ALD cycles of SiO_2. The mechanisms of H-bonded OH groups on the heterostructures are complex and not comparable with inclusion of more SiO_2. Heterostructures with identical cycle ratios follow a similar trend at 3650 cm^{-1} with a little deviation due to the different number of cycles of SiO_2 and HfO_2.

3.3. Atomic Force Microscopy Investigations

To further understand the evolution of surface roughness on such coatings, AFM inspections were performed on selected compositions. Figure 11 shows the surface roughness values of the samples along with two extreme AFM micrographs. Single-layer HfO_2 film has a maximum rms roughness value of about 1.07 nm, whereas heterostructure [8:2]*300 shows about 0.34 nm of rms surface roughness, implying fabrication of smooth multilayer stacks. Further, the heterostructures with [2:2]*615 and [16:16]*72 indicate rms roughness of about 0.96 and 0.60 nm, respectively. In general, more SiO_2 content decreases the surface roughness. However, the number of interfaces may also lead to higher roughness values, as observed in the case of [2:2]*615 heterostructure. Thick SiO_2 coatings have low surface roughness, and the quality of the ALD ultrathin coatings of silica is beneficial to reduce the surface roughness of the rougher hafnia [51,60].
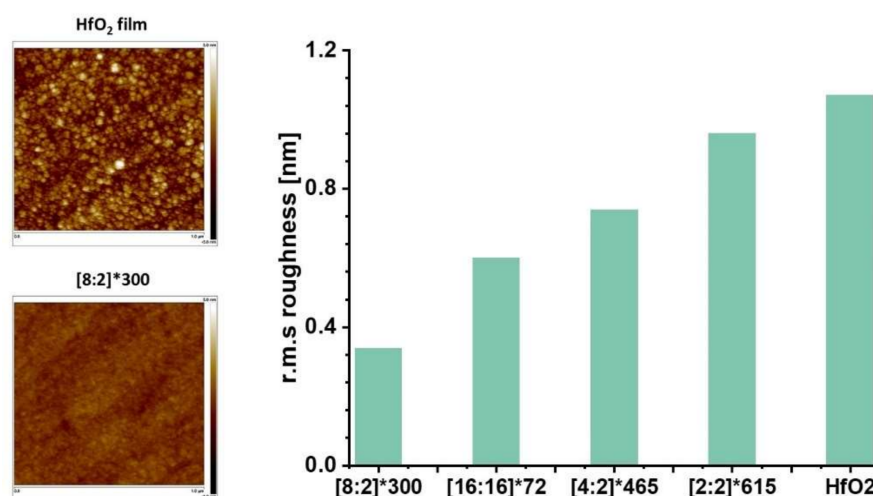

Figure 11. Surface roughness (rms) values of SiO_2:HfO_2 heterostructures in comparison to a single-layer HfO_2 film. The corresponding AFM micrographs are included.

3.4. Damage Performance of SiO_2:HfO_2 Heterostructures

SiO_2:HfO_2 heterostructure films grown on fused silica substrate were characterized by irradiation of nanosecond laser pulses using the R-on-1 method because of the limited number of test sites available on the substrates (small substrate area). The LIDT test is governed by test parameters that can influence the damage resistance of the coatings. Such parameters for Nd:YAG laser applied on R-on-1 test methods are specified in Table 3.

Table 3. LIDT test parameters for nanosecond laser at 355 nm wavelength.

Wavelength	Pulse Length	Repetition Rate	Incident Angle	Spot Diameter	Test Method
355 nm	7 ns	10 Hz	10°	200 to 300 μm	R-on-1

The damage test was initially conducted on single-layer HfO_2 and SiO_2 films. SiO_2 coatings evaluated here experienced damage immediately after laser irradiation due to coating defects. However, silica films are well-known to exhibit high LIDT due to the wide bandgap [89–91] and further analysis is required to study the formation of defects in PEALD coatings. The damage threshold of the HfO_2 film was estimated at 16 J/cm² through regression analysis. Zhang et al. reported an LIDT of 7 J/cm² [308 nm, 20 ns] grown by electron beam evaporation process [5]. They observed that HfO_2 deposited by ALD results in 31.8 J/cm² at 1064 nm wavelength with 3 ns pulses. Liu et al. also reported an LIDT of 14 J/cm² [S-on-1, 1064 nm, 10 ns] for HfO_2 grown by ALD [50]. The LIDT was different in the UV and NIR spectral range due to the different laser conditioning parameters,

test methods, as well as deposition processes [3,39,92,93]. The LIDT directly scales with the wavelength, even if the remaining laser parameters, test methods, and deposition process remain unchanged. Additionally, the pulse duration has a major influence on the damage mechanism.

The damage threshold of the heterostructures was between 20 and 79 J/cm^2 while increasing with SiO$_2$ content. In the nanosecond pulse regime, the LIDT is also influenced by the optical bandgap, i.e., the absorption edge. HfO$_2$ is the LIDT limiting material for the heterostructures in the UV spectral range because of its absorption edge. LIDT as a function of the optical bandgap of the heterostructures is shown in Figure 12a. Heterostructure [8:2]*300 exhibits a relatively higher LIDT of about 79 J/cm^2 while incorporating more SiO$_2$ content in the heterostructure, hence ensuring higher optical bandgap. The heterostructures with identical cycle ratios, such as [2:2]*615 and [16:16]*72, demonstrate LIDT in a similar range with slight deviations that are within the error margin. Heterostructure [2:16]*98, composed of higher relative content of HfO$_2$, reveals 20 J/cm^2, which is comparable with a single layer HfO$_2$ if the error margins are considered. Overall, the heterostructure film exhibits much higher LIDT than the single-layer HfO$_2$ films.
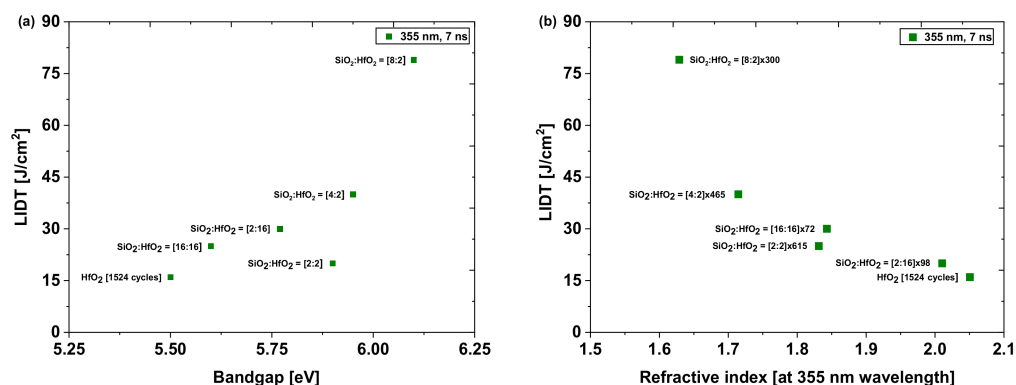

Figure 12. (**a**) LIDT vs. bandgap of various SiO$_2$:HfO$_2$ heterostructures; (**b**) LIDT vs. refractive indices of various SiO$_2$:HfO$_2$ heterostructures.

The LIDT in the nanosecond regime can also be explained in terms of refractive indices of SiO$_2$:HfO$_2$ heterostructures. The evolution of LIDT as a function of the tailored refractive indices obtained from heterostructure films is represented in Figure 12b, indicating an inverse relationship between them at 355 nm wavelength. Heterostructure [8:2]*300, having the highest optical bandgap and lowest surface roughness, exhibits the highest LIDT of 79 J/cm^2 (the lowest refractive index) due to the inclusion of more SiO$_2$ in the composition. An opposite scenario is noticeable for the [2:16]*98 heterostructure, where the refractive indices are much higher due to the inclusion of more HfO$_2$. The heterostructures with identical cycle ratios are also consistent with such refractive indices. HfO$_2$ as a high-index material reported the lowest LIDT of 16 J/cm^2 in this study.

The damage resistance of the heterostructures also depends on the absorption because it may degrade the functionality of the films by introducing defects. The absorption measurements on the heterostructures were conducted using the photothermal common-path interferometry (PCI) method. The LIDT vs. absorption of selected heterostructures are depicted in Figure 13. HfO$_2$ shows 278 ppm absorption at 355 nm wavelength which is significantly higher than for SiO$_2$ of about 4.5 ppm for thick coatings, as HfO$_2$ is an absorbing material in the UV spectral range. HfO$_2$ is the high-index material in the heterostructure, consequently has a relatively low optical bandgap. The LIDT of materials scales linearly with the optical bandgap values, hence, the LIDT of the SiO$_2$:HfO$_2$ heterostructures are limited by the HfO$_2$ content.
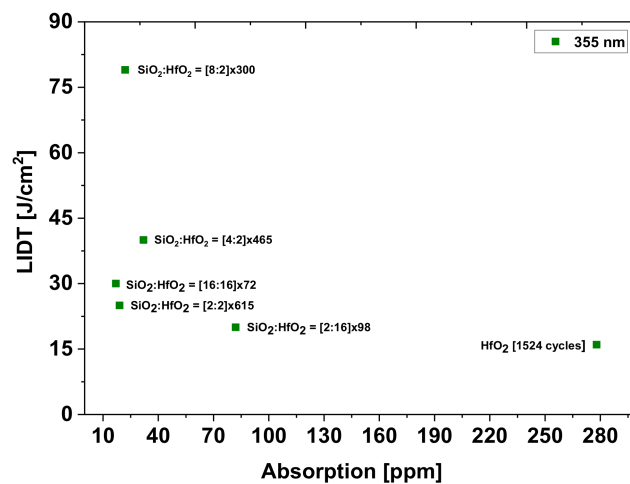
Figure 13. The effect of absorption on LIDT of selected heterostructures.

The heterostructures with more HfO_2 experience high absorption and comparatively low LIDT such as the [2:16]*98 heterostructure (82 ppm, 20 J/cm^2). The scenario is exactly the opposite for the [8:2]*300 and [4:2]*465 heterostructures where the LIDT is much higher with low absorption (addition of more SiO_2). Interestingly, the absorption losses have been significantly decreased in the heterostructures compared to pure HfO_2.

3.5. Antireflection Coatings

The antireflection (AR) coatings designed at 355 nm wavelength will be reported in this section. The heterostructures exhibit low optical absorption losses in the UV spectral range. The multilayer stack of discrete and heterostructure AR coatings will be demonstrated. Heterostructure coatings are also known as graded-index or rugate coatings, where refractive indices are varied along with the interlayer thickness, which can be obtained by adjusting the constituents cycle ratio of the heterostructures. The coatings were designed using the software OptiLayer, version 12.83 g (OptiLayer GmbH, Garching, Germany), whereby HfO_2 and SiO_2 were used as the high- and low-refractive-index material, respectively. The coatings were optimized between 0° and 45° angle of incidence. The design pattern for a multilayer coatings stack is provided in Table 4. The four-layer coatings start with an HfO_2 layer on the substrate followed by two alternating layers and ends with a SiO_2 layer. The corresponding refractive index profile of the design is illustrated in Figure 14. The coatings were designed for a total thickness of 152.3 nm.

Table 4. Design of multilayer stack antireflection coatings at 355 nm wavelength.

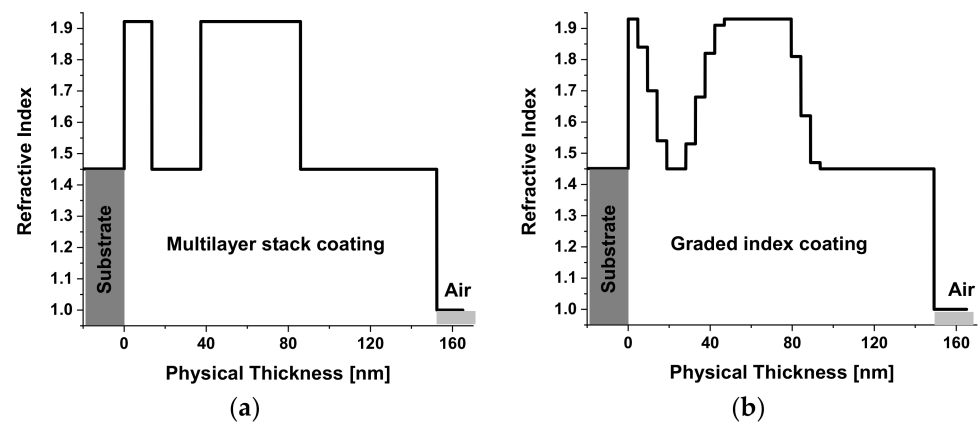| Layer	Material	Physical Thickness (nm)	Optical Thickness (nm)	Refractive Index
1	HfO_2	13.5	26.1	1.93
2	SiO_2	23.8	34.6	1.45
3	HfO_2	48.6	93.9	1.93
4	SiO_2	66.4	96.4	1.45
-	-	Total = 152.3	-	-

Figure 14. Refractive index profile of (**a**) multilayer stack and (**b**) graded index antireflection coatings at 355 nm.

The refractive indices of the intermediate layers vary due to the distinct composition cycle ratio of SiO_2 and HfO_2. In comparison to the multilayer stack, the graded coatings incorporate interlayers between the discontinuous interfaces. The graded AR design was optimized for a total thickness of 149.1 nm and is provided in Table 5. The corresponding refractive index profile of the design is also provided in Figure 14.

Table 5. Design of graded-index antireflection coatings at 355 nm wavelength.

Layer	Material	Composition	Physical Thickness (nm)	Fraction of HfO_2 (%)	Refractive Index	Number of Cycles/ Bilayers
1	HfO_2	Single layer	4.7	100	1.93	29
2	SiO_2:HfO_2	4:8	4.7	82.57	1.84	3
3	SiO_2:HfO_2	8:8	4.7	51.71	1.70	2
4	SiO_2:HfO_2	8:2	4.7	18.23	1.54	4
5	SiO_2	Single layer	9.3	0	1.45	80
6	SiO_2:HfO_2	8:2	4.7	17.78	1.53	4
7	SiO_2:HfO_2	8:8	4.7	48.43	1.68	2
8	SiO_2:HfO_2	4:8	4.7	78.27	1.82	4
9	SiO_2:HfO_2	2:8	4.7	96.31	1.91	3
10	HfO_2	Single layer	32.6	100	1.93	201
11	SiO_2:HfO_2	4:8	4.7	76.04	1.81	3
12	SiO_2:HfO_2	8:4	4.7	35.63	1.62	3
13	SiO_2:HfO_2	64:2	4.7	4.26	1.47	1
14	SiO_2	Single layer	55.9	0	1.45	482
-	-	-	Total = 149.1	-	-	-

The spectra of the designed and measured reflectance for the two types of antireflection coatings are shown in Figure 15. The coatings on the double-sides (ds) fused silica substrates were designed and prepared at a center wavelength of 355 nm for 6° and 45° angle of incidence (AOI). In the case of multilayer stacks, the AR films on the ds-coated substrates were designed to achieve reflectance less than 0.35% at 355 nm wavelength (6° AOI). The measured spectra of the AR coatings were in good agreement with the designed reflectance minima. A similar scenario was observed for the reflectivity curves at 45° AOI. The graded-index layer coatings were designed to achieve reflectance less than 0.4% and 1% at 355 nm wavelength for 6° and 45° AOI, respectively. However, the shift in measured reflectance minima of the AR graded coatings at 45° AOI toward a higher wavelength range could be attributed to several factors. As these are multilayer coatings, especially for the complicated graded-index coating, thickness variations in each layer can end up producing a shift in reflectance. There is also a thickness non-uniformity of about 2%–3% across the 300 mm

area in the reaction chamber. Further recalculation on estimating the actual growth of the individual materials in the multilayer coatings can be performed, and optimization of the number of ALD cycles can be implemented to ensure superior agreement with the design and the coating.
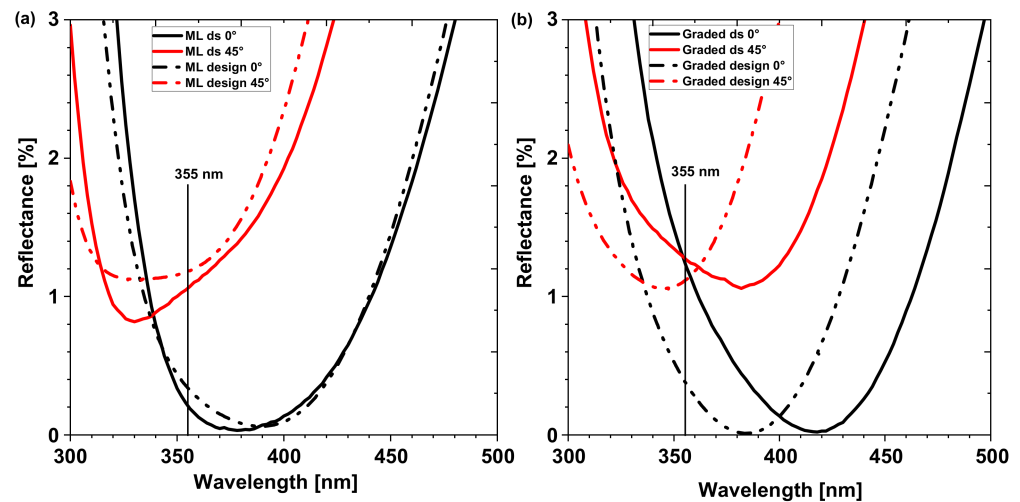

Figure 15. Comparison of designed and measured reflectance spectra for (**a**) multilayer stack and (**b**) graded antireflection coatings at 355 nm wavelength.

Laser damage resistance tests of the antireflection coatings at 355 nm wavelength were conducted using nanosecond laser pulses with a similar conditioning parameter of the R-on-1 method, as stated in Table 3. The LIDT of the AR coatings exhibits 29 ± 6 J/cm^2 and 31 ± 7 J/cm^2 for multilayer stack and graded structure, respectively, as mentioned in Table 6. The LIDT values of graded and multilayer stack coatings are comparable and differ by about 2 J/cm^2, which is within the measurement accuracy. Chaoyi et al. reported an LIDT of 24.4 J/cm^2 in the UV regime (355 nm wavelength) for HfO$_2$:SiO$_2$ films grown by the PEALD technique [1]. The laser damage threshold of graded-index coatings could have been much higher because of its robust design. Therefore, damage initiation mechanisms in the UV regime for nanosecond laser pulses might be linked to absorbing defects in the coatings [94,95].

Table 6. Absorption measurements for AR coatings at 355 nm wavelength.

Type of Coating	Method: PCI (Unannealed) (ppm)	Method: LID (Unannealed) (ppm)	Method: LID (Annealed) (ppm)	LIDT (J/cm^2)
Multilayer stack	16.7 ± 5.1	86.5 ± 2.2	26.5 ± 3.5	29 ± 6
Rugate coating	10.2 ± 3.2	85.3 ± 8.0	58.0 ± 7.5	31 ± 7

Absorption measurements on the AR coatings were carried out at 355 nm wavelength by using the photothermal common-path interferometry (PCI) and laser-induced deflection (LID) methods. The absorption values obtained from these techniques are summarized in Table 6. Measurements using the PCI technique provide a difference of 6.5 ppm between the graded and multilayer stack [50]. This method considered coatings that did not undergo annealing at a higher temperature. In the case of LID, the measurements were conducted at the same wavelength for both annealed and unannealed coatings, which provide significant differences in absorption. For the unannealed coatings, the absorption values are comparable with graded and multilayer stacks except for the errors. This is not the case for the annealed coatings since the absorption for rugate (58 ± 7.5 ppm) is approximately double compared to multilayer stack (26.5 ± 3.5 ppm). The absorption for both coatings

decreased significantly because of annealing, which indicates the presence of hydroxyl groups in the thin-film coatings. Therefore, annealing reveals a substantial reduction in weak absorption in the coatings and can increase the LIDT. The LIDT estimated in our case is applicable to unannealed coatings only. However, annealing at a high temperature can also transform the amorphous phase of the coating materials, such as HfO_2 into a crystalline state. The absorption values determined using PCI and LID techniques show significant differences, which could be an area of further research. The measurement threshold ranges for these techniques might also be different owing to the asymmetrical calibration methods of the systems.

4. Conclusions

In this work, we carried out a comprehensive study on the optical properties of SiO_2:HfO_2 heterostructures developed by the PEALD method between approximately 125 nm and 1000 nm in wavelength. Precise tuning of compositions enables tailoring of the refractive indices, extinction coefficients, and optical bandgaps of the heterostructure films. The optical bandgaps of the materials show an inverse relationship with the refractive indices at the reported wavelengths. A major limitation for optical applications is the low bandgap of the HfO_2 pure layers. By adding SiO_2 in the heterostructures, the optical bandgap is increased, and the optical losses are significantly decreased. This comes at the cost of a lower refractive index of the heterostructure compared to the pure HfO_2. FTIR studies on the heterostructures revealed larger absorbance due to OH groups in SiO_2 compared to HfO_2. XRR studies revealed layer-by-layer growth with ultrathin films of sub-nm thicknesses. The small surface roughness of the heterostructures indicates that the coatings were very smooth and amorphous. LIDT tests of the heterostructures were carried out using nanosecond pulses by employing the R-on-1 method. The LIDT of the he-terostructures was in good agreement with the literature for nanosecond pulses using the R-on-1 test method. The LIDT of the heterostructures in the nanosecond pulse regime can be scaled with their bandgap and refractive indices. Absorption played an additional role in damage estimation of such coatings because the LIDT was decreased significantly with increased absorption losses. The absorption in the HfO_2 films was higher in the UV regime because of its absorption edges. Two types of antireflection coatings (multilayer stacks and graded-index structures) were developed for high-power laser applications in the UV spectral range. The graded-index coatings were designed to reduce the effects of discontinuous interfaces (by incorporating intermediate layers) in the coatings. However, graded-index coatings could not significantly enhance the LIDT of the heterostructures in the ns-pulse regime. Further studies in the fs-pulse regime are planned with LIDT more sensitive to absorption. Several factors, such as conditioning of laser parameters and shifting of electric field distributions to low-index material from the layer interfaces (vulnerable to incident laser intensity) through sophisticated designs, will also be considered. High-reflection coatings ($\lambda/4$ optical thickness) and functionalization of 3D optical surfaces can be developed by ALD, and their LIDT will be examined in the future. Precise tuning of compositions enables tailoring of optical dispersion spectra. This enables artificially engineering new optical materials with an optimal combination of refractive index, bandgap, and LIDT values for high-power laser applications. Overall, this work demonstrates a possible route via PEALD to develop atomically thin heterostructures of SiO_2:HfO_2 with significantly tailored optical properties compared to the individual constituents.

Institutional Review Board Statement: Not applicable.

Informed Consent Statement: Not applicable.

Data Availability Statement: Not applicable.

Conflicts of Interest: The authors declare no conflict of interest.

References

1. Yin, C.; Zhu, M.; Zeng, T.; Song, C.; Chai, Y.; Shao, Y.; Zhang, R.; Zhao, J.; Li, D.; Shao, J. HfO_2/SiO_2 anti-reflection films for UV lasers via plasma-enhanced atomic layer deposition. *J. Alloy. Compd.* **2021**, *859*, 157875. [CrossRef]
2. Torchio, P.; Gatto, A.; Alvisi, M.; Albrand, G.; Kaiser, N.; Amra, C. High-reflectivity HfO_2/SiO_2 ultraviolet mirrors. *Appl. Opt.* **2002**, *41*, 3256–3261. [CrossRef] [PubMed]
3. Shahrokhabadi, H.; Vaezzadeh, M.; Bananej, A.; Maleki, M.H. Band gap energy and refractive index dependence of femtosecond laser induced damage threshold in dielectric thin films. *Thin Solid Film.* **2017**, *636*, 289–295. [CrossRef]
4. Li, C.; Zhao, Y.A.; Cui, Y.; Wang, Y.; Peng, X.; Shan, C.; Zhu, M.; Wang, J.; Shao, J. Investigation on picosecond laser-induced damage in HfO_2/SiO_2 high-reflective coatings. *Opt. Laser Technol.* **2018**, *106*, 372–377. [CrossRef]
5. Zhang, Q.; Pan, F.; Luo, J.; Wu, Q.; Wang, Z.; Wei, Y. Optical and laser damage properties of HfO_2/Al_2O_3 thin films deposited by atomic layer deposition. *J. Alloy. Compd.* **2016**, *659*, 288–294. [CrossRef]
6. Yuan, L.; Zhao, Y.; Shang, G.; Wang, C.; He, H.; Shao, J.; Fan, Z. Comparison of femtosecond and nanosecond laser-induced damage in HfO_2 single-layer film and HfO_2-SiO_2 high reflector. *J. Opt. Soc. Am. B* **2007**, *24*, 538. [CrossRef]
7. Pervak, V.; Krausz, F.; Apolonski, A. Hafnium oxide thin films deposited by reactive middle-frequency dual-magnetron sputtering. *Thin Solid Film.* **2007**, *515*, 7984–7989. [CrossRef]
8. Gallais, L.; Commandré, M. Laser-induced damage thresholds of bulk and coating optical materials at 1030 nm, 500 fs. *Appl. Opt.* **2014**, *53*, A186–A196. [CrossRef] [PubMed]
9. Bartzsch, H.; Lange, S.; Frach, P.; Goedicke, K. Graded refractive index layer systems for antireflective coatings and rugate filters deposited by reactive pulse magnetron sputtering. *Surf. Coat. Technol.* **2004**, *180–181*, 616–620. [CrossRef]
10. Hussin, R.; Choy, K.L.; Hou, X.H. Fabrication of Multilayer $ZnO/TiO_2/ZnO$ Thin Films with Enhancement of Optical Properties by Atomic Layer Deposition (ALD). *AMM* **2013**, *465–466*, 916–921. [CrossRef]
11. Vargas, M.; Murphy, N.R.; Ramana, C.V. Structure and optical properties of nanocrystalline hafnium oxide thin films. *Opt. Mater.* **2014**, *37*, 621–628. [CrossRef]
12. Lo Nigro, R.; Schilirò, E.; Mannino, G.; Di Franco, S.; Roccaforte, F. Comparison between thermal and plasma enhanced atomic layer deposition processes for the growth of HfO_2 dielectric layers. *J. Cryst. Growth* **2020**, *539*, 125624. [CrossRef]
13. Gallais, L.; Mangote, B.; Zerrad, M.; Commandré, M.; Melninkaitis, A.; Mirauskas, J.; Jeskevic, M.; Sirutkaitis, V. Laser-induced damage of hafnia coatings as a function of pulse duration in the femtosecond to nanosecond range. *Appl. Opt.* **2011**, *50*, C178–C187. [CrossRef]
14. Abromavičius, G.; Kičas, S.; Buzelis, R. High temperature annealing effects on spectral, microstructural and laser damage resistance properties of sputtered HfO_2 and HfO_2-SiO_2 mixture-based UV mirrors. *Opt. Mater.* **2019**, *95*, 109245. [CrossRef]
15. Al-Kuhaili, M.F. Optical properties of hafnium oxide thin films and their application in energy-efficient windows. *Opt. Mater.* **2004**, *27*, 383–387. [CrossRef]
16. Aarik, J.; Mändar, H.; Kirm, M.; Pung, L. Optical characterization of HfO_2 thin films grown by atomic layer deposition. *Thin Solid Film.* **2004**, *466*, 41–47. [CrossRef]
17. Padma Kumar, H.; Vidya, S.; Saravana Kumar, S.; Vijayakumar, C.; Solomon, S.; Thomas, J.K. Optical properties of nanocrystalline HfO_2 synthesized by an auto-igniting combustion synthesis. *J. Asian Ceram. Soc.* **2015**, *3*, 64–69. [CrossRef]
18. Robertson, J. High dielectric constant oxides. *Eur. Phys. J. Appl. Phys.* **2004**, *28*, 265–291. [CrossRef]
19. Kim, K.-M.; Jang, J.S.; Yoon, S.-G.; Yun, J.-Y.; Chung, N.-K. Structural, Optical and Electrical Properties of HfO_2 Thin Films Deposited at Low-Temperature Using Plasma-Enhanced Atomic Layer Deposition. *Materials* **2020**, *13*, 2008. [CrossRef]
20. Zhao, C.; Zhao, C.Z.; Werner, M.; Taylor, S.; Chalker, P. Dielectric relaxation of high-k oxides. *Nanoscale Res. Lett.* **2013**, *8*, 456. [CrossRef]
21. Golosov, D.A.; Vilya, N.; Zavadski, S.M.; Melnikov, S.N.; Avramchuk, A.V.; Grekhov, M.M.; Kargin, N.I.; Komissarov, I.V. Influence of film thickness on the dielectric characteristics of hafnium oxide layers. *Thin Solid Film.* **2019**, *690*, 137517. [CrossRef]
22. Gao, L.; Lemarchand, F.; Lequime, M. Refractive index determination of SiO_2 layer in the UV/Vis/NIR range: Spectrophotometric reverse engineering on single and bi-layer designs. *J. Eur. Opt. Soc. Rapid Publ.* **2013**, *8*, 13010. [CrossRef]
23. Liu, H. Atomic Layer Deposition for High Power Laser Applications: Al_2O_3 and HfO_2. Ph.D. Dissertation, Leibniz University, Hannover, Germany, 2018.

24. Kamiyama, S.; Miura, T.; Nara, Y. Comparison between SiO$_2$ films deposited by atomic layer deposition with SiH$_2$[N(CH$_3$)$_2$]$_2$ and SiH[N(CH$_3$)$_2$]$_3$ precursors. *Thin Solid Film.* **2006**, *515*, 1517–1521. [CrossRef]

25. Choi, D.-w.; Chung, K.-B.; Park, J.-S. Rapid vapor deposition SiO$_2$ thin film deposited at a low temperature using tris(tert-pentoxy)silanol and trimethyl-aluminum. *Mater. Chem. Phys.* **2013**, *142*, 614–618. [CrossRef]

26. Das, N.C.; Sahoo, N.K.; Bhattacharyya, D.; Thakur, S.; Kamble, N.M.; Nanda, D.; Hazra, S.; Bal, J.K.; Lee, J.F.; Tai, Y.L.; et al. Correlation between local structure and refractive index of e-beam evaporated (HfO$_2$–SiO$_2$) composite thin films. *J. Appl. Phys.* **2010**, *108*, 23515. [CrossRef]

27. Dingemans, G.; van Helvoirt, C.; van de Sanden, M.C.M.; Kessels, W.M. Plasma-Assisted Atomic Layer Deposition of Low Temperature SiO$_2$. *ECS Trans.* **2011**, *35*, 191–204. [CrossRef]

28. Pfeiffer, K.; Shestaeva, S.; Bingel, A.; Munzert, P.; Ghazaryan, L.; van Helvoirt, C.; Kessels, W.M.M.; Sanli, U.T.; Grévent, C.; Schütz, G.; et al. Comparative study of ALD SiO$_2$ thin films for optical applications. *Opt. Mater. Express* **2016**, *6*, 660. [CrossRef]

29. Ashraf, N.S.; Alam, S.; Alam, M. *New Prospects of Integrating Low Substrate Temperatures with Scaling-Sustained Device Architectural Innovation*; Morgan & Claypool Publishers: San Rafael, CA, USA, 2016; ISBN 9781627058551.

30. Fabien, P. Plasma Assisted Chemical Deposition (CVD/ALD) and Integration of Ti(Al)N and Ta(Al)N for Sub-20 nm Metal Gate. Ph.D. Dissertation, Université de Grenoble, Grenoble, France, 2014.

31. Li, D.-H.; Zhai, C.-H.; Zhou, W.-C.; Huang, Q.-H.; Wang, L.; Zheng, H.; Chen, L.; Chen, X.; Zhang, R.-J. Effects of Bilayer Thickness on the Morphological, Optical, and Electrical Properties of Al$_2$O$_3$/ZnO Nanolaminates. *Nanoscale Res. Lett.* **2017**, *12*, 563. [CrossRef]

32. Mende, M.; Schrameyer, S.; Ehlers, H.; Ristau, D.; Gallais, L. Laser damage resistance of ion-beam sputtered Sc$_2$O$_3$/SiO$_2$ mixture optical coatings. *Appl. Opt.* **2013**, *52*, 1368–1376. [CrossRef]

33. Fu, X.; Melnikaitis, A.; Gallais, L.; Kiáčas, S.; Drazdys, R.; Sirutkaitis, V.; Commandré, M. Investigation of the distribution of laser damage precursors at 1064 nm, 12 ns on niobia-silica and zirconia-silica mixtures. *Opt. Express* **2012**, *20*, 26089–26098. [CrossRef]

34. Jena, S.; Tokas, R.B.; Kamble, N.M.; Thakur, S.; Sahoo, N.K. Optical properties and laser damage threshold of HfO$_2$-SiO$_2$ mixed composite thin films. *Appl. Opt.* **2014**, *53*, 850–860. [CrossRef] [PubMed]

35. Kukli, K.; Kemell, M.; Castán, H.; Dueñas, S.; Seemen, H.; Rähn, M.; Link, J.; Stern, R.; Ritala, M.; Leskelä, M. Atomic Layer Deposition and Properties of HfO$_2$-Al$_2$O$_3$ Nanolaminates. *ECS J. Solid State Sci. Technol.* **2018**, *7*, P501–P508. [CrossRef]

36. Kukli, K.; Kemell, M.; Heikkilä, M.J.; Castán, H.; Dueñas, S.; Mizohata, K.; Ritala, M.; Leskelä, M. Silicon oxide-niobium oxide mixture films and nanolaminates grown by atomic layer deposition from niobium pentaethoxide and hexakis(ethylamino) disilane. *Nanotechnology* **2020**, *31*, 195713. [CrossRef] [PubMed]

37. Jensen, L.O.; Mende, M.; Blaschke, H.; Ristau, D.; Nguyen, D.; Emmert, L.; Rudolph, W. Investigations on SiO$_2$/HfO$_2$ mixtures for nanosecond and femtosecond pulses. In *Laser-Induced Damage in Optical Materials: 2010, Proceedings of the Laser Damage Symposium XLII: Annual Symposium on Optical Materials for High Power Lasers, Boulder, CO, USA, 26–29 September 2010*; Exarhos, G.J., Gruzdev, V.E., Menapace, J.A., Ristau, D., Soileau, M.J., Eds.; SPIE: Bellingham, WA, USA, 2010; p. 784207.

38. Stolz, C.J.; Caputo, M.; Griffin, A.J.; Thomas, M.D. BDS thin film UV antireflection laser damage competition. In *Laser-Induced Damage in Optical Materials: 2010, Proceedings of the Laser Damage Symposium XLII: Annual Symposium on Optical Materials for High Power Lasers, Boulder, CO, USA, 26–29 September 2010*; Exarhos, G.J., Gruzdev, V.E., Menapace, J.A., Ristau, D., Soileau, M.J., Eds.; SPIE: Bellingham, WA, USA, 2010; p. 784206.

39. Yu, Z.; He, H.; He, K.; Qi, H.; Wei, S.; Chen, S. Mechanism for defect dependence of damage morphology in HfO$_2$/SiO$_2$ high reflectivity coating under nanosecond ultraviolet laser irradiation. *Optik* **2014**, *125*, 5323–5326. [CrossRef]

40. Pu, Y.; Ma, P.; Chen, S.; Zhu, J.; Wang, G.; Pan, F.; Sun, P.; Zhu, X.; Zhu, J.; Xiao, D. Mechanism for atmosphere dependence of laser damage morphology in HfO$_2$/SiO$_2$ high reflective films. *J. Appl. Phys.* **2012**, *112*, 23111. [CrossRef]

41. Pu, Y.; Ma, P.; Lv, L.; Zhang, M.; Lu, Z.; Qiao, Z.; Qiu, F. Enhanced thermomechanical stability on laser-induced damage by functionally graded layers in quasi-rugate filters. *Appl. Surf. Sci.* **2018**, *440*, 288–293. [CrossRef]

42. Li, Y.; Shen, W.; Hao, X.; Lang, T.; Jin, S.; Liu, X. Rugate notch filter fabricated by atomic layer deposition. *Appl. Opt.* **2014**, *53*, A270–A275. [CrossRef]

43. Tikhonravov, A.V.; Trubetskov, M.K.; Amotchkina, T.V.; Kokarev, M.A.; Kaiser, N.; Stenzel, O.; Wilbrandt, S.; Gäbler, D. New optimization algorithm for the synthesis of rugate optical coatings. *Appl. Opt.* **2006**, *45*, 1515–1524. [CrossRef]

44. Schwartzberg, A.M.; Olynick, D. Complex Materials by Atomic Layer Deposition. *Adv. Mater.* **2015**, *27*, 5778–5784. [CrossRef]

45. Zhang, J.-C.; Xiong, L.-M.; Fang, M.; He, H.-B. Wide-angle and broadband graded-refractive-index antireflection coatings. *Chin. Phys. B* **2013**, *22*, 44201. [CrossRef]

46. Herffurth, T.; Trost, M.; Schröder, S.; Täschner, K.; Bartzsch, H.; Frach, P.; Duparré, A.; Tünnermann, A. Roughness and optical losses of rugate coatings. *Appl. Opt.* **2014**, *53*, A351–A359. [CrossRef] [PubMed]

47. Shi, S.; Qian, S.; Hou, X.; Mu, J.; He, J.; Chou, X. Structural and Optical Properties of Amorphous Al$_2$O$_3$ Thin Film Deposited by Atomic Layer Deposition. *Adv. Condens. Matter Phys.* **2018**, *2018*, 1–10. [CrossRef]

48. Taylor, L.N.; Brown, A.K.; Pung, A.J.; Johnson, E.G.; Talghader, J.J. Continuous-wave laser damage of uniform and nanolaminate hafnia and titania optical coatings. *Opt. Lett.* **2013**, *38*, 4292–4295. [CrossRef] [PubMed]

49. Khoshman, J.M.; Khan, A.; Kordesch, M.E. Amorphous hafnium oxide thin films for antireflection optical coatings. *Surf. Coat. Technol.* **2008**, *202*, 2500–2502. [CrossRef]

50. Liu, H.; Ma, P.; Pu, Y.; Zhao, Z. Atomic layer deposition of Al_2O_3 and HfO_2 for high power laser application. *J. Alloy. Compd.* **2021**, *859*, 157751. [CrossRef]

51. Lapteva, M.; Beladiya, V.; Riese, S.; Hanke, P.; Otto, F.; Fritz, T.; Schmitt, P.; Stenzel, O.; Tünnermann, A.; Szeghalmi, A. Influence of temperature and plasma parameters on the properties of PEALD HfO_2. *Opt. Mater. Express* **2021**, *11*, 1918. [CrossRef]

52. Nguyen, N.V.; Davydov, A.V.; Chandler-Horowitz, D.; Frank, M.M. Sub-bandgap defect states in polycrystalline hafnium oxide and their suppression by admixture of silicon. *Appl. Phys. Lett.* **2005**, *87*, 192903. [CrossRef]

53. Neumayer, D.A.; Cartier, E. Materials characterization of ZrO_2–SiO_2 and HfO_2–SiO_2 binary oxides deposited by chemical solution deposition. *J. Appl. Phys.* **2001**, *90*, 1801–1808. [CrossRef]

54. Kariniemi, M.; Niinistö, J.; Vehkamäki, M.; Kemell, M.; Ritala, M.; Leskelä, M.; Putkonen, M. Conformality of remote plasma-enhanced atomic layer deposition processes: An experimental study. *J. Vac. Sci. Technol. A Vac. Surf. Film.* **2012**, *30*, 01A115. [CrossRef]

55. Chaaya, A.A.; Viter, R.; Baleviciute, I.; Bechelany, M.; Ramanavicius, A.; Gertnere, Z.; Erts, D.; Smyntyna, V.; Miele, P. Tuning Optical Properties of Al_2O_3/ZnO Nanolaminates Synthesized by Atomic Layer Deposition. *J. Phys. Chem. C* **2014**, *118*, 3811–3819. [CrossRef]

56. Mitchell, D.R.G.; Triani, G.; Attard, D.J.; Finnie, K.S.; Evans, P.J.; Barbé, C.J.; Bartlett, J.R. Atomic layer deposition of TiO_2 and Al_2O_3 thin films and nanolaminates. *Smart Mater. Struct.* **2006**, *15*, S57–S64. [CrossRef]

57. Homola, T.; Buršíková, V.; Ivanova, T.V.; Souček, P.; Maydannik, P.S.; Cameron, D.C.; Lackner, J.M. Mechanical properties of atomic layer deposited Al_2O_3/ZnO nanolaminates. *Surf. Coat. Technol.* **2015**, *284*, 198–205. [CrossRef]

58. Liu, Z.; Chen, S.; Ma, P.; Wei, Y.; Zheng, Y.; Pan, F.; Liu, H.; Tang, G. Characterization of 1064 nm nanosecond laser-induced damage on antireflection coatings grown by atomic layer deposition. *Opt. Express* **2012**, *20*, 854–863. [CrossRef] [PubMed]

59. Liu, H.; Jensen, L.; Ma, P.; Ristau, D. ALD anti-reflection coatings at 1ω, 2ω, 3ω, and 4ω for high-power ns-laser application. *Adv. Opt. Technol.* **2018**, *7*, 23–31. [CrossRef]

60. Beladiya, V.; Becker, M.; Faraz, T.; Kessels, W.M.M.E.; Schenk, P.; Otto, F.; Fritz, T.; Gruenewald, M.; Helbing, C.; Jandt, K.D.; et al. Effect of an electric field during the deposition of silicon dioxide thin films by plasma enhanced atomic layer deposition: An experimental and computational study. *Nanoscale* **2020**, *12*, 2089–2102. [CrossRef] [PubMed]

61. Potts, S.E.; Keuning, W.; Langereis, E.; Dingemans, G.; van de Sanden, M.C.M.; Kessels, W.M.M. Low Temperature Plasma-Enhanced Atomic Layer Deposition of Metal Oxide Thin Films. *J. Electrochem. Soc.* **2010**, *157*, P66. [CrossRef]

62. Mäkelä, M.; Hatanpää, T.; Mizohata, K.; Meinander, K.; Niinistö, J.; Räisänen, J.; Ritala, M.; Leskelä, M. Studies on Thermal Atomic Layer Deposition of Silver Thin Films. *Chem. Mater.* **2017**, *29*, 2040–2045. [CrossRef]

63. Van Beekum, E.R.J. PEALD and PECVD Inorganic Layers: Microstructure Characterization and Moisture Permeation Barrier Properties. Master's Thesis, Eindhoven University of Technology, Eindhoven, The Netherlands, 2012.

64. Stenzel, O.; Wilbrandt, S.; Friedrich, K.F.; Kaiser, N. Realistische Modellierung der NIR/VIS/UV-optischen Konstanten dünner optischer Schichten im Rahmen des Oszillatormodells. *VIP* **2009**, *21*, 15–23. [CrossRef]

65. Amotchkina, T.V.; Trubetskov, M.K.; Tikhonravov, A.V.; Janicki, V.; Sancho-Parramon, J.; Razskazovskaya, O.; Pervak, V. Oscillations in spectral behavior of total losses ($1-R-T$) in thin dielectric films. *Opt. Express* **2012**, *20*, 16129–16144. [CrossRef]

66. Tikhonravov, A.V.; Trubetskov, M.K.; Amotchkina, T.V.; DeBell, G.; Pervak, V.; Sytchkova, A.K.; Grilli, M.L.; Ristau, D. Optical parameters of oxide films typically used in optical coating production. *Appl. Opt.* **2011**, *50*, C75–C85. [CrossRef]

67. Gottwald, A.; Kroth, U.; Richter, M.; Schöppe, H.; Ulm, G. Ultraviolet and vacuum-ultraviolet detector-based radiometry at the Metrology Light Source. *Meas. Sci. Technol.* **2010**, *21*, 125101. [CrossRef]

68. Gottwald, A.; Wiese, K.; Siefke, T.; Richter, M. Validation of thin film TiO_2 optical constants by reflectometry and ellipsometry in the VUV spectral range. *Meas. Sci. Technol.* **2019**, *30*, 45201. [CrossRef]

69. Ardigo, M.R.; Ahmed, M.; Besnard, A. Stoney Formula: Investigation of Curvature Measurements by Optical Profilometer. *AMR* **2014**, *996*, 361–366. [CrossRef]

70. Nakanishi, S.; Kojima, R.; Kozuka, H. In-plane stress development in sol–gel-derived titania and silica thin films on Si(100) substrates. *J. Sol-Gel Sci. Technol.* **2020**, *93*, 506–516. [CrossRef]

71. Besnard, A.; Ardigo, M.R.; Imhoff, L.; Jacquet, P. Curvature radius measurement by optical profiler and determination of the residual stress in thin films. *Appl. Surf. Sci.* **2019**, *487*, 356–361. [CrossRef]

72. Vargas, M. Nanometric Structure-Property Relationship in Hafnium Oxide Thin Films Made by Sputter-Deposition. Master's Thesis, University of Texas, El Paso, TX, USA, 2014.

73. Wang, R. Nanostructuring and Understanding Nanostructuring and Understanding Morphology-Property Correlation in Semiconductor Thin Films. Ph.D. Dissertation, Technical University of Munich, Munich, Germany, 2018.

74. Alqaheem, Y.; Alomair, A.A. Microscopy and Spectroscopy Techniques for Characterization of Polymeric Membranes. *Membranes* **2020**, *10*, 33. [CrossRef]

75. Petrović, V. Boronic Acids in Molecular Layer Deposition. Master's Thesis, University of Oslo, Oslo, Norway, 2019.

76. Stratan, A.; Zorila, A.; Rusen, L.; Simion, S.; Blanaru, C.; Fenic, C.; Neagu, L.; Nemes, G. Automated test station for laser-induced damage threshold measurements according to ISO 21254-1,2,3,4 standards. *Laser-Induc. Damage Opt. Mater.* **2012**, *8530*, 85301Y. [CrossRef]

77. Velpula, P.K.; Kramer, D.; Rus, B. Femtosecond Laser-Induced Damage Characterization of Multilayer Dielectric Coatings. *Coatings* **2020**, *10*, 603. [CrossRef]

78. Knoops, H.C.M.; Potts, S.E.; Bol, A.A.; Kessels, W.M.M. Atomic Layer Deposition. In *Handbook of Crystal Growth*; Elsevier: Amsterdam, The Netherlands, 2015; pp. 1101–1134. ISBN 9780444633040.

79. Abromavičius, G. Microstructural and Optical Properties of Metal Oxide Optical Coatings Deposited by Ion Beam Sputtering and Their Application in UV Spectral Range. Ph.D. Dissertation, Vilnius University, Vilnius, Lithuania, 2020.

80. Marine, C. Study of High Damage Threshold Optical Coatings Used in environment with Very Low Hygrometry for Fusion Class Laser System. Ph.D. Dissertation, University of Bordeaux, Bordeaux, France, 2019.

81. Angelov, I.B.; von Pechmann, M.; Trubetskov, M.K.; Krausz, F.; Pervak, V. Optical breakdown of multilayer thin-films induced by ultrashort pulses at MHz repetition rates. *Opt. Express* **2013**, *21*, 31453–31461. [CrossRef]

82. Oliver, J.B. Evaporated HfO_2/SiO_2 Optical Coatings and Modifications for High-Power Laser Applications. Ph.D. Dissertation, University of Rochester, New York, NY, USA, 2012.

83. Jinman, G.; Junhong, S.; Lei, C.; Junqi, X. Influence of Substrate Surface Properties on Laser-induced Damage Properties of TiO_2 Thin Films. *IJM* **2016**, *10*, 1–10. [CrossRef]

84. Paul, P.; Hafiz, M.G.; Schmitt, P.; Patzig, C.; Otto, F.; Fritz, T.; Tünnermann, A.; Szeghalmi, A. Optical bandgap control in Al_2O_3/TiO_2 heterostructures by plasma enhanced atomic layer deposition: Toward quantizing structures and tailored binary oxides. *Spectrochim. Acta A Mol. Biomol. Spectrosc.* **2021**, *252*, 119508. [CrossRef]

85. Puurunen, R.L.; Delabie, A.; van Elshocht, S.; Caymax, M.; Green, M.L.; Brijs, B.; Richard, O.; Bender, H.; Conard, T.; Hoflijk, I.; et al. Hafnium oxide films by atomic layer deposition for high-κ gate dielectric applications: Analysis of the density of nanometer-thin films. *Appl. Phys. Lett.* **2005**, *86*, 73116. [CrossRef]

86. Buiu, O.; Davey, W.; Lu, Y.; Mitrovic, I.Z.; Hall, S. Ellipsometric analysis of mixed metal oxides thin films. *Thin Solid Film.* **2008**, *517*, 453–455. [CrossRef]

87. Aygun, G.; Yildiz, I. Interfacial and structural properties of sputtered HfO_2 layers. *J. Appl. Phys.* **2009**, *106*, 14312. [CrossRef]

88. Zeng, T.; Zhu, M.; Chai, Y.; Yin, C.; Xu, N.; Yi, K.; Wang, Y.; Zhao, Y.; Hu, G.; Shao, J. Effects of water adsorption on properties of electron-beam HfO_2/SiO_2 high-reflection coatings. *Thin Solid Film.* **2020**, *697*, 137826. [CrossRef]

89. Kumar, S.; Shankar, A.; Kishore, N.; Mukherjee, C.; Kamparath, R.; Thakur, S. Laser-induced damage threshold study on TiO_2/SiO_2 multilayer reflective coatings. *Indian J. Phys.* **2020**, *94*, 105–115. [CrossRef]

90. Mangote, B.; Gallais, L.; Commandré, M.; Mende, M.; Jensen, L.; Ehlers, H.; Jupé, M.; Ristau, D.; Melninkaitis, A.; Mirauskas, J.; et al. Femtosecond laser damage resistance of oxide and mixture oxide optical coatings. *Opt. Lett.* **2012**, *37*, 1478–1480. [CrossRef] [PubMed]

91. Kong, P.; Pu, Y.; Ma, P.; Zhu, J. The characterization and properties of mixed Sc_2O_3/SiO_2 films. *Thin Solid Film.* **2020**, *714*, 138357. [CrossRef]

92. Zhao, Y.; Wang, T.; Zhang, D.; Shao, J.; Fan, Z. Laser conditioning and multi-shot laser damage accumulation effects of HfO_2/SiO_2 antireflective coatings. *Appl. Surf. Sci.* **2005**, *245*, 335–339. [CrossRef]

93. Bananej, A.; Hassanpour, A.; Razzaghi, H.; Vaez zade, M.; Mohammadi, A. The effect of porosity on the laser induced damage threshold of TiO_2 and ZrO_2 single layer films. *Opt. Laser Technol.* **2010**, *42*, 1187–1192. [CrossRef]

94. Liu, M.; He, G.; Zhu, L.Q.; Fang, Q.; Li, G.H.; Zhang, L.D. Microstructure and interfacial properties of $HfO_2–Al_2O_3$ nanolaminate films. *Appl. Surf. Sci.* **2006**, *252*, 6206–6211. [CrossRef]

95. Zhao, Y.; Gao, W.; Shao, J.; Fan, Z. Roles of absorbing defects and structural defects in multilayer under single-shot and multi-shot laser radiation. *Appl. Surf. Sci.* **2004**, *227*, 275–281. [CrossRef]